Available online at www.sciencedirect.com
ScienceDirect
Trans. Nonferrous Met. Soc. China 35(2025) 4266−4280
Transactions of Nonferrous Metals Society of China
www.tnmsc.cn

Self-oxidation among iron-bearing minerals promoting magnetite formation from pyrite in Bayer liquor

Zhao-hua ZENG, Gui-hua LIU, Tian-gui QI, Lei-ting SHEN, Qiu-sheng ZHOU, Zhi-hong PENG, Yi-lin WANG, Xiao-bin LI

School of Metallurgy and Environment, Central South University, Changsha 410083, China

Received 26 April 2024; accepted 27 December 2024

Abstract: The effects of siderite, hematite, and goethite on pyrite reactions in sodium aluminate solution at high temperatures, based on the coexistence of pyrite and iron-bearing minerals in bauxite, were studied. The addition of siderite, goethite, and hematite increases the concentrations of $S_2O_3^{2-}$, SO_3^{2-} and SO_4^{2-}, enhancing sulfur removal during desilication. Siderite and hematite facilitate nearly 100% magnetite formation from pyrite, whereas goethite leads to the formation of both hematite and magnetite from pyrite through a multiphase transformation process. Iron-bearing minerals significantly increase the iron content in residues and enhance iron recovery from the red mud. Siderite, goethite, and hematite produce a porous surface in the form of erosive holes due to electrochemical corrosion, improving reaction efficiency of pyrite. Additionally, electrochemical corrosion promotes the pyrite reaction in accordance with the Kröger and Ziegler models, controlled by interfacial diffusion and chemical reactions in the presence of siderite, hematite and magnetite.

Key words: pyrite; self-oxidation; iron-bearing minerals; magnetite; sodium aluminate solution

1 Introduction

Pyrite (FeS_2) frequently occurs alongside metal ores such as copper [1], zinc, and gold, generating acid mine drainage (AMD) during the excavation of abandoned mines and tunnels [2]. Pyrite also contributes to acid rain through SO_2/SO_3 during ore processing [3]. In high-sulfur bauxite, pyrite exacerbates the corrosion of steel equipment, increases alkali soda loss, deteriorates the separation of the red mud, and contaminates alumina, limiting the utilization of 1.5×10^9 t of bauxite with a high sulfur content (>0.7 wt.%) in China. Moreover, iron recovery from the 30%−60% Fe_2O_3 present in the red mud is generally low due to the weak magnetism of hematite and goethite [4]. Therefore, efficient sulfur removal from Bayer liquor (sodium aluminate solution) and improved iron recovery from red mud are critical to alumina production.

Roasting and flotation are commonly used in alumina refineries to remove sulfur from bauxite [5]. However, the high cost, high energy consumption, and large volume of SO_2 associated with roasting, as well as the negative effects of organics on alumina production, tremendous amounts of attached water, and the complexity of the flotation process, have limited their widespread adoption. Furthermore, sulfur remains in the bauxite concentrate (sulfur content <0.3 wt.%), leading to the accumulation of sulfur anions in the Bayer liquor, which adversely impacts alumina production.

As S^{2-}, $S_2O_3^{2-}$, SO_3^{2-} and SO_4^{2-} generally coexisted in the sodium aluminate solution after

Corresponding author: Gui-hua LIU, E-mail: liugh303@csu.edu.cn
https://doi.org/10.1016/S1003-6326(25)66943-3

bauxite containing sulfur was digested by the Bayer process [6], various approaches for sulfur removal from the sodium aluminate solution were studied. Precipitation of S^{2-} using zinc [7] and sodium ferrite [8], and SO_4^{2-} by adding $Ba(OH)_2$ [9], has been reported. Oxidation by pumping O_2 [10] or adding $NaNO_3$ [11] to a sodium aluminate solution has also been used to transform S^{2-} into $S_2O_3^{2-}$, SO_3^{2-} and SO_4^{2-}. However, the use of expensive additives, complex processes, and the decline in alumina quality have limited their applications. In addition, the weak magnetism of hematite and goethite in red mud results in low iron recovery efficiency (<35%) and iron content in concentrates (TFe <55%), which have long impeded the economic utilization of red mud for decades. Moreover, sulfur species such as $S_2O_3^{2-}$, SO_3^{2-} and SO_4^{2-} are easily incorporated into zeolite (desilication product, PSD) [12]. This study introduces a novel self-oxidation approach that eliminates negative S^{2-} from pyrite by converting it into $S_2O_3^{2-}$, SO_3^{2-}, and SO_4^{2-}, while simultaneously promoting Fe_3O_4 formation to enhance iron recovery from red mud.

The reaction between pyrite and iron-bearing minerals in the sodium aluminate solution is crucial for digestion in the Bayer process. Fe^{3+}/Fe^{2+} ions from iron-bearing minerals, which act as oxidants, readily react with pyrite under acidic conditions [13,14]. Meanwhile, higher temperature, lower S^{2-} concentration, and increased caustic soda concentration promote pyrite reactions [15,16]. 40%−90% of pyrite is digested into the sodium aluminate solution during the Bayer process, and magnetite forms on the surface of pyrite, inhibiting further reaction [17]. Hematite can be converted to magnetite by controlling the redox potential [18], and the addition of hematite seeds promotes the conversion of goethite to hematite at high temperatures in the sodium aluminate solution [19]. However, few studies have reported the self-oxidation of pyrite and iron-bearing minerals from bauxite in the sodium aluminate solution at high temperatures using the Bayer process.

In this study, the self-oxidation reactions between pyrite and iron-bearing minerals were investigated based on the coexistence of hematite, goethite, and siderite with pyrite in bauxite. The thermodynamics of these reactions were first examined, followed by a study of the effects of hematite, goethite, and siderite on pyrite reactions. Phase transformation, iron content, and morphology of the residues after digestion were carefully examined. Finally, the reaction mechanism was discussed based on the kinetic model and scanning electron microscopy (SEM) images. The results provide insight into the self-oxidation mechanism between pyrite and iron-bearing minerals in alkaline solutions and suggest new opportunities for the economical utilization of high-sulfur bauxite.

2 Experimental

2.1 Materials

Pyrite was purchased from Yunnan Province, China. The pyrite was soaked in a 6 mol/L HCl solution at room temperature for 48 h and then washed with deionized water [20]. The treated pyrite was dried at 45 °C. X-ray diffraction (XRD) patterns of the resulting pyrite and iron-bearing minerals are shown in Fig. 1. All peaks corresponding to FeS_2 in Fig. 1 were assigned to pyrite (PDF No. 97-063-3274), with a composition of 50.94% Fe, and 44.58% S, yielding a S/Fe molar ratio of 2.0, confirming the presence of the pure pyrite. SEM images of the pyrite and iron-bearing minerals (hematite, goethite, and siderite) are shown in Fig. 2. The particle sizes of pyrite and siderite are less than 15 μm, whereas those of hematite and goethite are less than 5 μm, as shown in Fig. S1 of Supporting Material (SM).

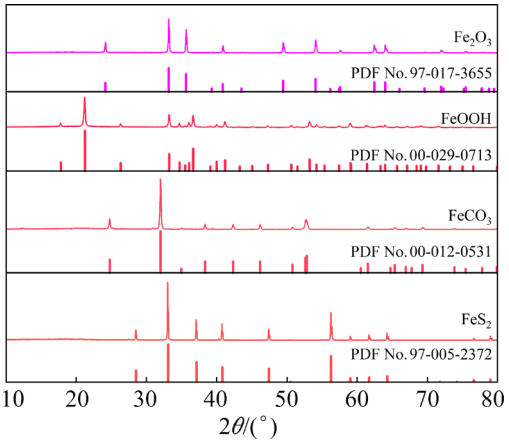

Fig. 1 XRD patterns of pyrite after wet pretreatment with 6 mol/L HCl and iron-bearing minerals

Sodium aluminate solution was prepared by dissolving aluminum hydroxide and sodium hydroxide in hot deionized water. Based on the composition of Bayer liquor during the digestion

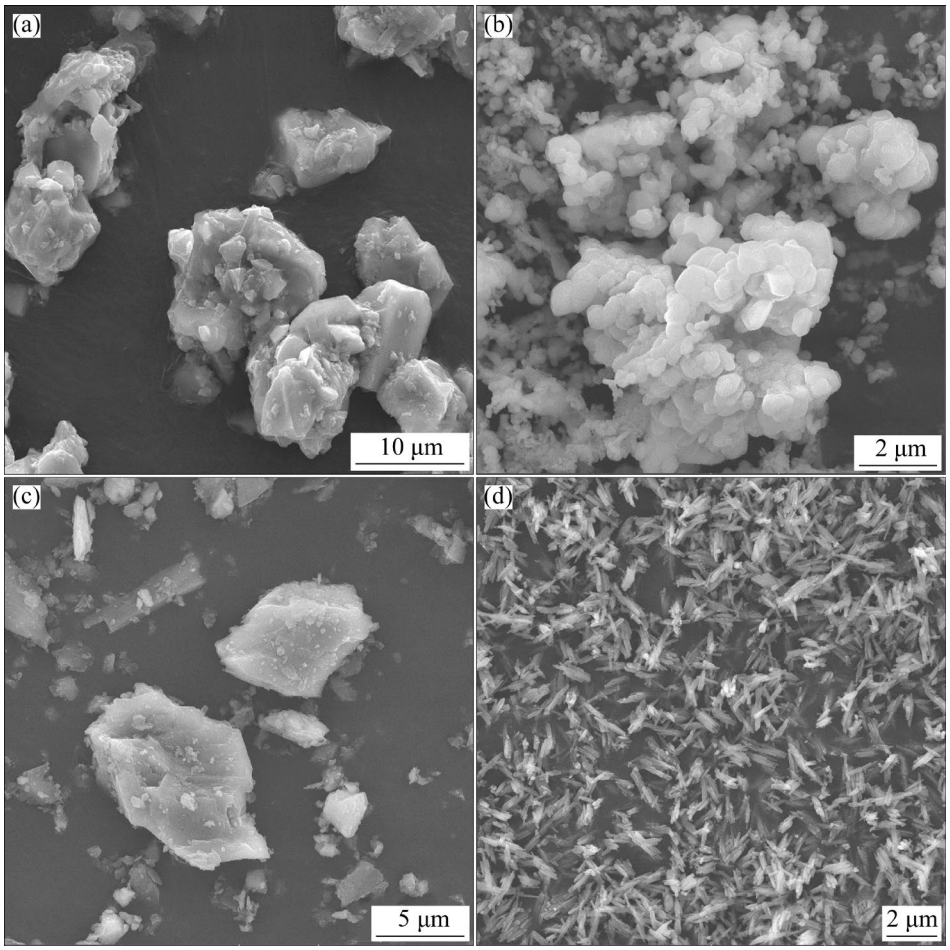

Fig. 2 SEM images of minerals: (a) Pyrite; (b) Hematite; (c) Siderite; (d) Goethite

process, the composition of the as-synthesized sodium aluminate solution contained 230 g/L Na_2O and 126 g/L Al_2O_3, with α_k=3.0 (molar ratio of Na_2O to Al_2O_3 in solution).

Hematite, siderite, goethite, $Al(OH)_3$, NaOH, and other reagents used in this study were of analytical grade and purchased from Sinopharm Chemical Reagent Co., Ltd.

2.2 Procedure

Sodium aluminate solution (100 mL), pyrite, and iron-bearing minerals were added into a 150 mL steel bomb. Four steel balls (2×*d*15 mm and 2×*d*5 mm) were added to intensify the agitation. After sealing the bomb, digestion was carried out in molten salt at high temperatures [21]. The bomb was subsequently cooled rapidly with water, and the resulting slurry was filtered. The filter cake was washed with boiling water and dried at 50 °C for 36 h. The dried cake was then used to record XRD patterns and SEM images. The filtrate was used to determine the concentration of sulfur-containing ions.

2.3 Characterization and methods

XRD patterns of the minerals and residues were recorded using a D/Max 2500VB (Rigaku Corporation, Japan) with Cu K_α radiation at a scanning rate of 5 (°)/min. Phase content was semi-quantitatively analyzed using the RIR method [22]. SEM (MIRA3-LMH, TESCAN, Czech Republic) and energy-dispersive X-ray spectroscopy (EDX) (One Max20, Czech Republic) were used to determine microscopic morphology and microscale composition (EDS mapping). Sulfur content in the pyrite and residues was detected using a sulfur analyzer (HDS3000, Hunan Huade Electronics Corporation, China) [23]. Concentrations (generally expressed as S) of $S_2O_3^{2-}$, SO_3^{2-} and SO_4^{2-} were determined by ion chromatography (ICS-90A, Dionex, USA) [24], whereas S^{2-} concentration was measured using titration method [25]. Iron content in the residues was determined using the potassium dichromate titration method (GB/T 6730.65—2009). Fe(II) and Fe(III) concentrations (generally expressed as Fe_2O_3) in the solution were measured

using iron-phenanthroline spectrophotometry (HJ/T 345—2007).

The oxidation proportion (R_S) was determined using Eq. (1):

$$R_S=\frac{C_2+C_3+C_4}{C_1+C_2+C_3+C_4}\times 100\% \quad (1)$$

where C_1, C_2, C_3 and C_4 represent the concentrations of S^{2-}, $S_2O_3^{2-}$, SO_3^{2-} and SO_4^{2-}, respectively.

The reaction efficiency (η_S) of pyrite can be calculated using Eq. (2):

$$\eta_S=\left(1-\frac{m_2x_2}{m_1x_1}\right)\times 100\% \quad (2)$$

where m_1 and m_2 respectively represent the mass of the pyrite and residues, and x_1 and x_2 represent the mass fraction of sulfur in the pyrite and residues, respectively.

3 Thermodynamic reactions of pyrite, hematite, goethite and siderite during digestion

High temperatures and concentrated caustic soda were used during digestion. The possible reactions involving iron-bearing minerals are presented in Table 1. Sulfur (S_2^{2-}) in pyrite may be converted into S^{2-}, SO_4^{2-}, SO_3^{2-} and $S_2O_3^{2-}$, whereas the iron-bearing minerals may transform into Fe_3O_4 and Fe_2O_3.

Table 1 Chemical reactions of pyrite and iron-bearing minerals in Bayer digestion

No.	Reaction formula
(1)	$FeS_2+8/3OH^-=1/3Fe_3O_4+2/3S^{2-}+2/3S_2^{2-}+4/3H_2O$
(2)	$FeS_2+4OH^-=1/3Fe_3O_4+11/6S^{2-}+1/6SO_4^{2-}+2H_2O$
(3)	$FeS_2+4OH^-=1/3Fe_3O_4+16/9S^{2-}+2/9SO_3^{2-}+2H_2O$
(4)	$FeS_2+11/3OH^-=1/3Fe_3O_4+5/3S^{2-}+1/6S_2O_3^{2-}+11/6H_2O$
(5)	$FeS_2+8/3OH^-=1/3Fe_3O_4+4/3S^{2-}+2/3S+4/3H_2O$
(6)	$FeS_2+5OH^-=HFeO_2^-+7/4S^{2-}+1/4SO_4^{2-}+2H_2O$
(7)	$HFeO_2^-+1/3H_2O=1/3Fe_3O_4+OH^-+1/3H_2(g)\uparrow$
(8)	$FeCO_3+2OH^-=Fe(OH)_2+CO_3^{2-}$
(9)	$FeCO_3+2OH^-=1/3Fe_3O_4+CO_3^{2-}+2/3H_2O+1/3H_2(g)\uparrow$
(10)	$FeOOH=1/2Fe_2O_3+1/2H_2O$
(11)	$FeOOH+OH^-=FeO_2^-+H_2O$
(12)	$FeOOH+1/2HFeO_2^-=1/2Fe_3O_4+1/2H_2O+1/2OH^-$
(13)	$Fe_2O_3+HFeO_2^-=Fe_3O_4+OH^-$
(14)	$Fe_2O_3+2OH^-=FeO_2^-+H_2O$

Based on the possible reactions in Table 1 and the thermodynamic data listed in Table S1 of SM [26], the relationship between Gibbs free energy of reaction (ΔG^Θ) and T was calculated using Factsage 8.2, as illustrated in Fig. 3.

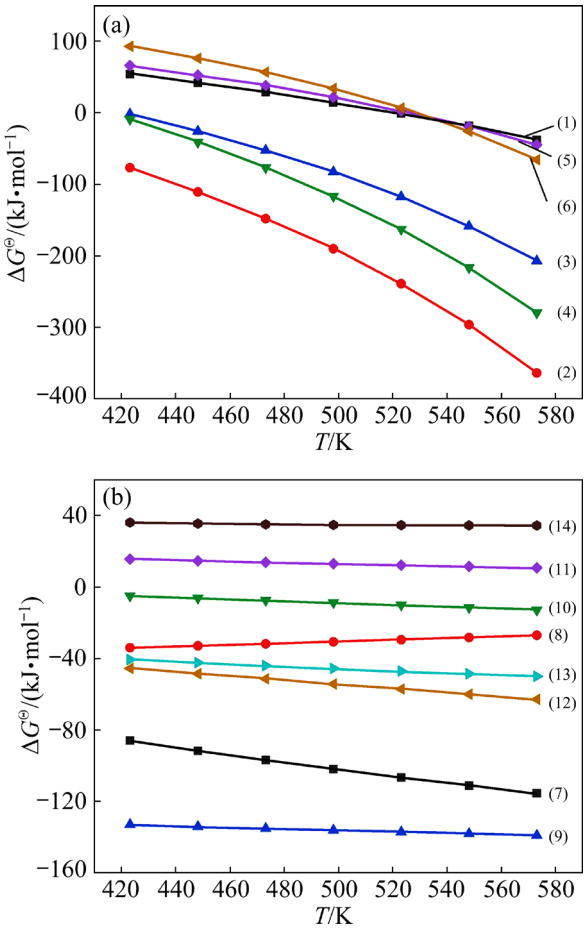

Fig. 3 Relationship between ΔG^Θ and T: (a) Pyrite; (b) Iron-bearing mineral

The digestion temperature in various stages of the Bayer process ranges from 503 to 553 K. As illustrated in Fig. 3, due to the negative Gibbs free energy of the reactions, species such as Fe_2O_3 along with Fe_3O_4, S^{2-}, $S_2O_3^{2-}$, SO_3^{2-} and SO_4^{2-} may form in the sodium aluminate solution. Meanwhile, pyrite may convert to Fe_3O_4, accompanied by the formation of $S_2O_3^{2-}$, SO_3^{2-} and SO_4^{2-} (Fig. 3(a)). Increasing the temperature may favor the formation of $HFeO_2^-$. However, FeOOH and Fe_2O_3 show resistance to conversion into FeO_2^- (Fig. 3(b)), whereas $HFeO_2^-$ and $FeCO_3$ preferentially transform into Fe_3O_4. Furthermore, Fe(II) in $FeCO_3$ and

$HFeO_2^-$ can convert into Fe_3O_4. It is important to note that sulfur species such as S and S_2^{2-} are unlikely to form in concentrated alkaline solutions at high temperatures, and FeO_2^- formation is minimal during digestion.

Thus, iron in pyrite may primarily transform into Fe_3O_4 and $HFeO_2^-$, whereas the sulfur may convert into S^{2-}, $S_2O_3^{2-}$, SO_3^{2-}, and SO_4^{2-}. The presence of $HFeO_2^-$ and $FeCO_3$ facilitates the formation of Fe_3O_4. These results imply that the self-oxidation of iron-bearing minerals and pyrite may occur.

4 Results and discussion

Based on the thermodynamic analysis, hematite, goethite, and siderite were added into the sodium aluminate solution during pyrite digestion. The study focused on the efficiency of the pyrite reaction, the presence of sulfur in the solution, iron concentration, phase evolution, and electrochemical corrosion.

4.1 Effect of iron-bearing minerals on pyrite reaction efficiency in digestion

The effects of temperature and reaction time on pyrite reaction efficiency are shown in Fig. 4. A significant increase in the efficiency of the pyrite reaction was observed with increasing temperature. Extending the reaction time initially resulted in a sharp increase in reaction efficiency, which later plateaued. Pyrite exhibited low reaction efficiency within the temperature range of 220−240 °C (Fig. 4(a)). For example, the reaction efficiency of pyrite was 55.46% at 260 °C, while a reaction efficiency greater than 95% was achieved at 280 °C within 30 min.

The addition of hematite, goethite, and siderite enhanced the reaction of pyrite, as shown in Figs. 4(b−d). More than 98% reaction efficiency was achieved at 280 °C, and the additives also accelerated the pyrite reaction within 10 min. The effects of the iron-bearing minerals on the pyrite reaction were different. For example, after 10 min at 220−280 °C, hematite increased reaction

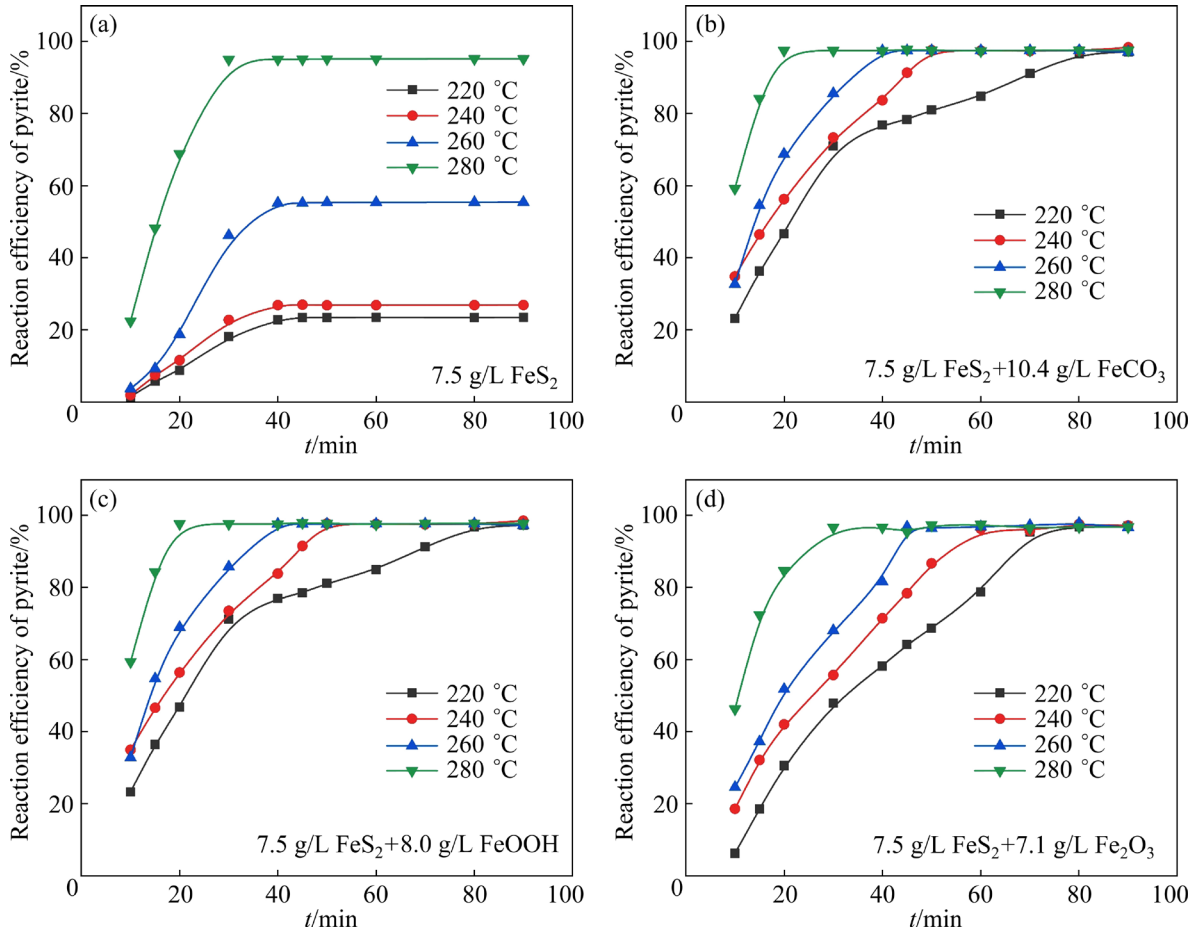

Fig. 4 Effect of temperature and reaction time on pyrite reaction efficiency in the presence of various iron-bearing minerals in sodium aluminate solution (Na_2O_k: 230 g/L; α_k: 3.0)

efficiency from 6.34% to 46.34%, while adding goethite increased reaction efficiency from 1.66% to 23.17% (Figs. 4(c, d)). In contrast, after siderite was added, the reaction efficiency of pyrite increased from 22.38% (before addition) to 59.29% after 10 min at 280 °C, and more than 98% of reaction efficiency was found within 20 min. Therefore, siderite remarkably promoted the pyrite reaction during digestion compared to hematite and goethite.

4.2 Effect of iron-bearing mineral dosage on pyrite reaction efficiency

Hematite and goethite are extensively found in bauxite, generally accounting for 1% to 15% Fe_2O_3. Siderite is also present in bauxite deposits in China and Guinea. The effect of iron-bearing mineral dosage (expressed as Fe) on pyrite reaction efficiency is shown in Fig. 5. As the dosages of hematite, goethite, and siderite increased, reaction efficiency increased sharply and then remained almost constant. Hematite and goethite dosages of 3 g/L resulted in reaction efficiencies of 86.03% and 84.95%, respectively, while siderite achieved a reaction efficiency of 98.27% at the same dosage. These results corroborate the findings shown in Fig. 4, where siderite significantly enhanced the pyrite reaction at 260 °C. Therefore, the difference in pyrite reaction efficiency during digestion can be attributed to the varying iron-bearing mineral contents in bauxite. These results imply that self-oxidation is significantly dependent on the presence of iron-bearing minerals.

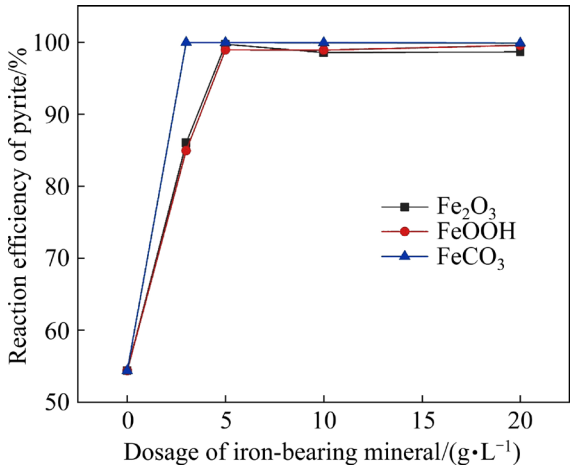

Fig. 5 Effect of iron-bearing mineral dosage on pyrite reaction efficiency in sodium aluminate solution (Na_2O_k: 230 g/L; α_k: 3.0) at 260 °C for 60 min

4.3 Effect of iron-bearing minerals on sulfur ions and iron concentrations in sodium aluminate solution

In practice, iron (expressed as Fe_2O_3) concentration is less than 20 mg/L in the Bayer liquor, which has a minimal impact on alumina quality. However, due to the formation of soluble $Na_2[FeS_2(OH)_2]$ and other soluble iron ions, a high concentration of Fe_2O_3 has been reported in some alumina refineries in China, where Fe_2O_3 content in alumina may reach 0.14 wt.%, exceeding the smelter-grade alumina specification of less than 0.02 wt.%. Therefore, it is crucial to understand the variation in sulfur ions and Fe_2O_3 concentration during digestion to economically remove sulfur from sodium aluminate solutions and produce high-quality alumina. Figure 6 shows the effect of iron-bearing minerals on the concentrations of S ions and Fe_2O_3.

When hematite, goethite, and siderite were not added, as shown in Figs. 6(a−c), the concentrations of S^{2-} and total sulfur (S_T) were 1.01 and 2.25 g/L, respectively. The concentrations of $S_2O_3^{2-}$, SO_3^{2-}, and SO_4^{2-} were all less than 0.3 g/L. The oxidation proportion (R_S) was approximately 25%. The addition of iron-bearing minerals increased S^{2-} and S_T concentrations in the pyrite reaction. However, the addition of iron-bearing minerals resulted in variations in the concentrations of sulfur ions and R_S. For example, increasing the dosage of siderite significantly increased the S^{2-} and S_T concentrations in the solution, whereas the concentrations of SO_4^{2-}, SO_3^{2-} and $S_2O_3^{2-}$ slowly increased. R_s decreased by approximately 15%, primarily due to the high reaction efficiency of pyrite. In contrast, increasing the dosage of hematite and goethite notably increased the concentrations of S^{2-} and S_T in the solution, which then stabilized (Figs. 6(b, c)), while the SO_4^{2-}, SO_3^{2-} and $S_2O_3^{2-}$ concentrations increased. However, R_S initially reduced but then increased significantly, surpassing 25% at 20 g/L of hematite and goethite. These results indicate that Fe(III) in hematite and goethite promotes the conversion of S^{2-} into SO_4^{2-}, SO_3^{2-} and $S_2O_3^{2-}$ compared to siderite.

In addition, Fe in the solution was predominantly present in the form of Fe(II) (Figs. 6(d−f)), with only a small amount of Fe(III) detected in the sodium aluminate solution. Without the addition of iron-bearing minerals, the

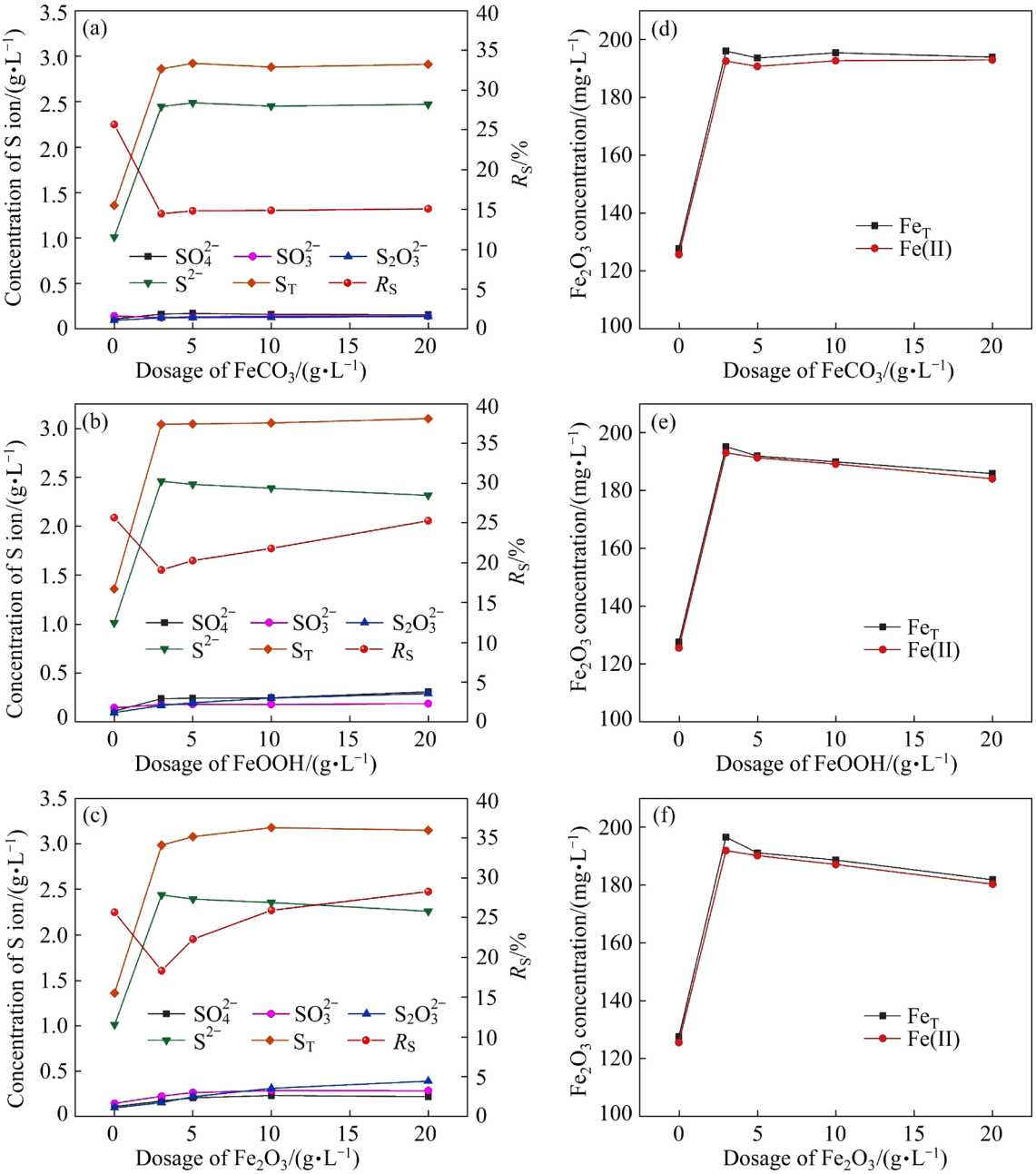

Fig. 6 Effect of iron-bearing mineral dosage on concentrations of S ions (a−c) and Fe_2O_3 (d−f) at 260 °C (Na_2O_k: 230 g/L; α_k: 3.0; 60 min)

concentrations of total iron (Fe_T) and Fe(II) were 127.64 and 125.63 mg/L, respectively. After adding 3 g/L of siderite, goethite, and hematite, Fe_T and Fe(II) concentrations exceeded 190 mg/L. These high concentrations of Fe(II) and Fe_T are mainly attributed to the formation of $Na_2[FeS_2(OH)_2]$, colloidal $Fe(OH)_2$, and $HFeO_2^-$ in solution, which facilitate magnetite formation. Furthermore, when the dosage of hematite and goethite exceeded 5 g/L, Fe(II) and Fe_T concentrations slightly decreased.

Notably, the variation in Fe(II) concentrations followed that of S^{2-}, indicating that S^{2-} concentrations are directly related to the concentration of Fe(II) in the solution [27,28]. These findings further confirm that the soluble $Na_2[FeS_2(OH)_2]\cdot 2H_2O$ mainly contributes to the Fe(II) and Fe_T concentrations.

4.4 Phase transformation and iron content in residues

4.4.1 Various phases in residues

Figure 7 displays XRD patterns of the residues after pyrite reacted with iron-bearing minerals at 260 °C. Regardless of the addition of iron-bearing

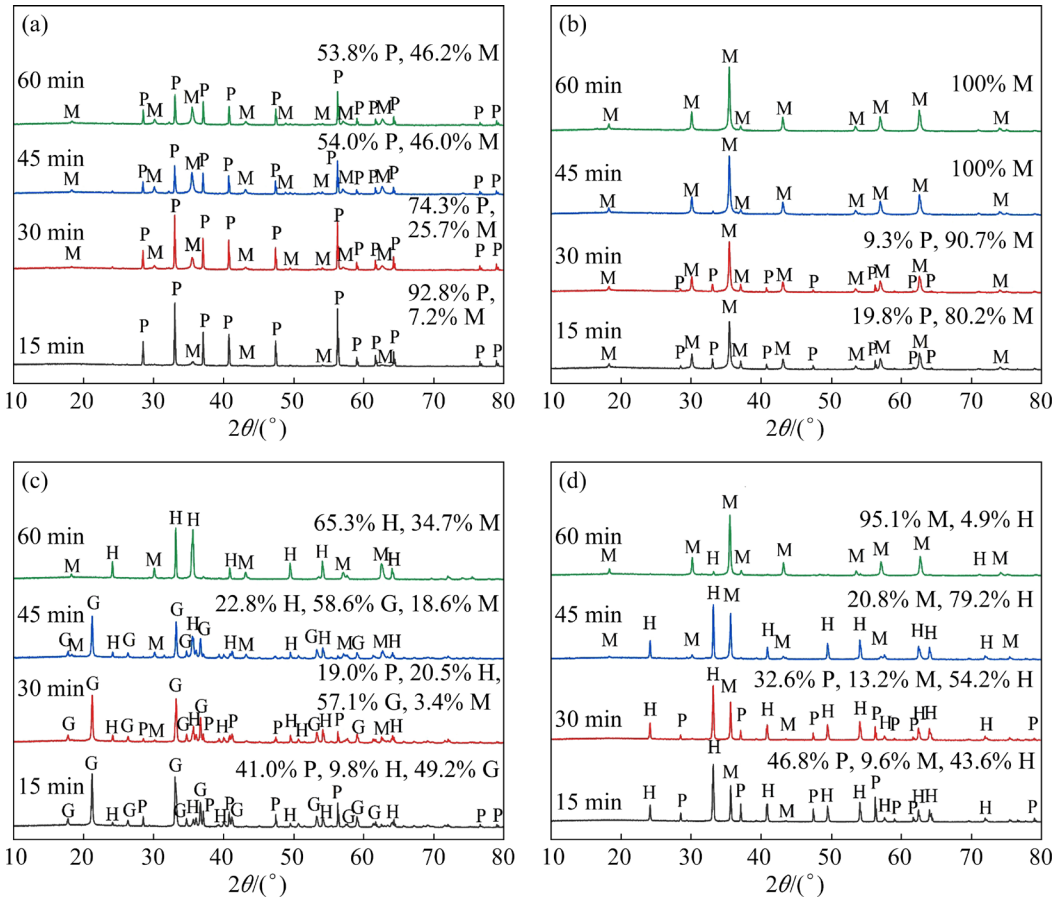

Fig. 7 XRD patterns of residues from pyrite reacting with iron-bearing minerals in sodium aluminate solution (Na_2O_k: 230 g/L; α_k: 3.0) at 260 °C (P−Pyrite; M−Magnetite; H−Hematite; G−Goethite): (a) 7.5 g/L FeS_2; (b) 7.5 g/L FeS_2 + 10.4 g/L $FeCO_3$; (c) 7.5 g/L FeS_2 + 8.0 g/L FeOOH; (d) 7.5 g/L FeS_2 + 7.1 g/L Fe_2O_3

minerals, the reaction of pyrite in the sodium aluminate solution generated magnetite, as shown in Table 1. This prolonged duration benefited magnetite formation. However, the magnetite content varied significantly after the addition of iron-bearing minerals. In the absence of additives, high pyrite and low magnetite contents were observed, with 54.0% and 53.8% pyrite remaining in the residues after digestion at 260 °C for 45 min, and 60 min, respectively. The low reaction efficiency is in good agreement with the results shown in Fig. 4(a).

Figure 7(b) shows a significant increase in magnetite content with the addition of siderite compared to the results in Fig. 7(a). After 45 min, only magnetite (100%) was observed, with no pyrite remaining. These results imply that siderite in bauxite notably promotes the formation of magnetite from Fe(II) in solution.

Similarly, the addition of goethite and hematite also promoted the pyrite reaction and magnetite formation (Figs. 7(c, d)). The magnetite contents in the residues at 60 min were 34.7% with goethite and 95.1% with hematite. However, these values were lower than those obtained with siderite. Based on pyrite reaction efficiency, the order of promotion by iron-bearing minerals is siderite >hematite > goethite.

4.4.2 Variation of iron content in residues

Iron recovery from the red mud has been performed extensively through magnetic separation in China and is notably dependent on the formation of magnetite. Meanwhile, the iron content in concentrates is crucial for the economic feasibility of iron recovery from the red mud. The results indicate that iron-bearing minerals favor the formation of magnetite, as evidenced by the high iron content (TFe 72.4%) in Fe_3O_4 compared to Fe_2O_3 (TFe 70.0%), FeOOH (TFe 62.9%), and FeS_2 (TFe 46.7%). The effects of iron-bearing minerals on the iron content of the residues are shown in Fig. 8.

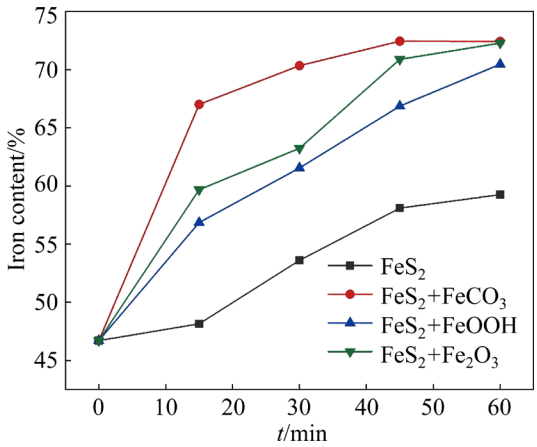

Fig. 8 Effect of iron-bearing minerals on iron content of residues in sodium aluminate solution at 260 °C

The iron content in the residues increased with time, aligning with the increasing proportion of magnetite (Fig. 7) and the reaction efficiency (Fig. 4). Notably, pyrite reacted with the sodium aluminate solution yielded a residue iron content of 59.26% at 60 min due to low reaction efficiency and the presence of pyrite in the residues. Adding siderite, hematite, and goethite significantly increased the iron content in the residues. For example, iron contents of 72.44%, 72.28%, and 70.46% in residues from adding siderite, hematite, and goethite were obtained at 60 min, respectively. Furthermore, adding siderite, hematite, and goethite also resulted in 72.44%, 70.38%, and 66.86% Fe in residue after 45 min. These results confirm that siderite promotes pyrite reaction in the sodium aluminate solution more effectively than hematite and goethite, suggesting that efficient iron recovery from the red mud can be achieved through self-oxidation during digestion. This provides a novel approach for simultaneously recovering iron from the red mud and removing sulfur from Bayer liquor in high-sulfur bauxite.

4.5 Effect of iron-bearing minerals on morphologies of residues after digestion

To better understand the effects of iron-bearing minerals on the reaction efficiency of pyrite and iron content in the residues, the morphological changes in the residues after digestion were discussed.

4.5.1 Morphology of residues from pyrite without iron-bearing minerals

The SEM images (Figs. 9(a–d)), EDS mapping (Figs. 9(e−g)), and elemental distribution (Fig. 9(h)) of the residues are presented in Fig. 9. No apparent changes in particle size (less than 15 μm) were observed on the surface of residues at 15 min (Fig. 9(a)). After 30 min, Fe_3O_4 particles (Spots 3# and 4#) began to appear (Fig. 9(h)) and by 45 min, many Fe_3O_4 particles had agglomerated into coarse particles (Figs. 9(c, d)). These coarse particles, wrapped in Fe_3O_4 (Spot 5#), possibly inhibited the pyrite reaction, as indicated by 55.46% of reaction

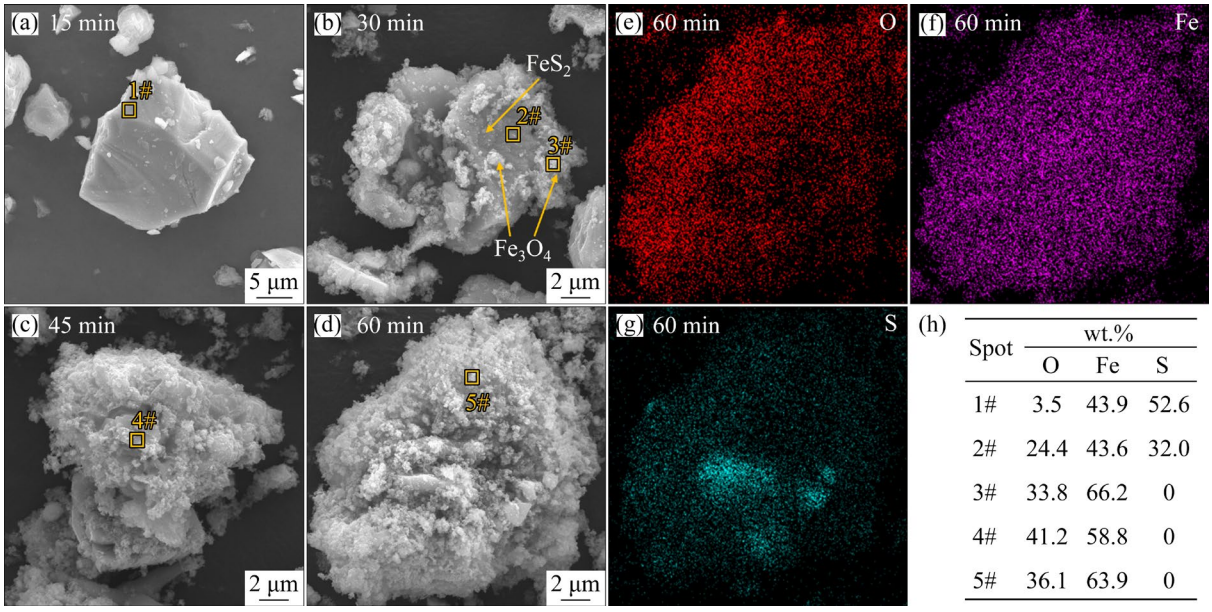

(h)

Spot	wt.%		
	O	Fe	S
1#	3.5	43.9	52.6
2#	24.4	43.6	32.0
3#	33.8	66.2	0
4#	41.2	58.8	0
5#	36.1	63.9	0

Fig. 9 SEM images (a−d), EDS mapping (e−g), and elemental distribution (h) of residues from pyrite in sodium aluminate solution (Na_2O_k: 230 g/L; α_k: 3.0) at 260 °C

efficiency shown in Fig. 4 and the 53.6% pyrite in the residues shown in Fig. 7.

Based on the *E*−pH diagram of the Na−S−Fe−H_2O system [29], the conversion of pyrite to Fe_3O_4 and $HFeO_2^-$ is advantageous. The S^{2-} and Fe(II) ions in the solution promoted the formation of Fe_3O_4, as shown in Table 1 and Fig. 3. Furthermore, Fe(II) in the sodium aluminate solution readily converts to Fe(III), generating H_2. The coexistence of Fe(II) and Fe(III) further promotes magnetite formation from pyrite (Reaction (7) in Table 1).

4.5.2 Morphologies of residues from pyrite with siderite addition

The addition of siderite resulted in the formation of numerous erosive holes, each less than 2 μm in diameter, on the surface of pyrite at 15 min (Fig. 10(a)), in contrast to the morphologies of residue from pyrite in Fig. 9. These rich holes in the pyrite particles generated a porous surface with a large specific surface area, thereby facilitating the pyrite reaction and promoting ionic diffusion. The formation of these erosive holes is attributed to electrochemical corrosion, likely induced by the low concentrations of Fe(III) (Fig. 6) reacting with S_2^{2-} on the pyrite surface. As the reaction progressed, a significant number of Fe_3O_4 particles were observed covering the pyrite (Spot 5#, Fig. 10(d)). After 45 min, pyrite was transformed into magnetite (Fig. 10(c)).

In alkaline solutions, CO_3^{2-} can form soluble iron-carbonate complexes ($Fe(CO_3)_2^{2-}$) in dilute alkaline solutions at normal temperatures, whereas Fe(II) and Fe(III) hydroxocomplexes in the form of soluble $Fe(OH)_4^-$ and $Fe(OH)_2$ are readily formed from $Fe(CO_3)_2^{2-}$ in concentrated alkaline solution [30]. Fe(II) may also exist as $HFeO_2^-$ [31]. Consequently, when siderite reacts rapidly with OH^-, some Fe(II) ions are oxidized to Fe(III), accompanied by the release of CO_3^{2-} and H_2 (Reaction (9) in Table 1). Subsequently, magnetite is generated. The high reaction efficiency of pyrite with the addition of siderite can be attributed to the synergistic contribution of soluble iron-bearing complexes and electrochemical corrosion.

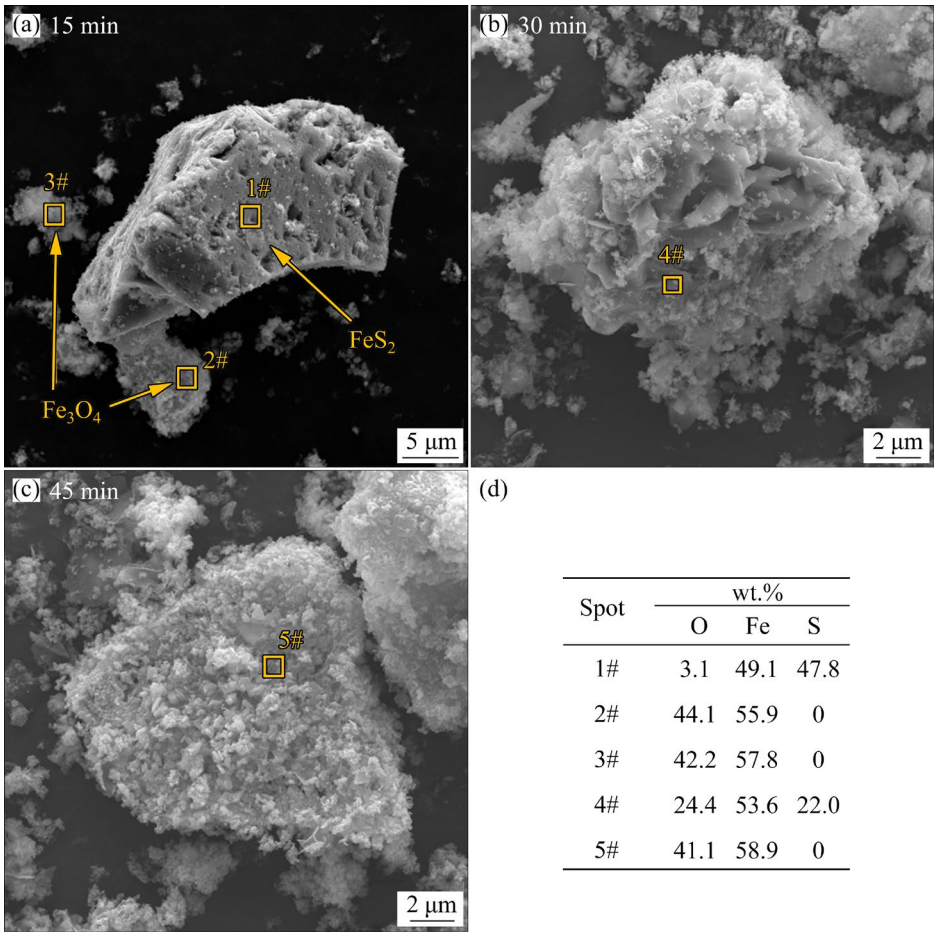

Spot	wt.%		
	O	Fe	S
1#	3.1	49.1	47.8
2#	44.1	55.9	0
3#	42.2	57.8	0
4#	24.4	53.6	22.0
5#	41.1	58.9	0

Fig. 10 SEM images (a−c) and elemental distribution (d) of residues from pyrite after siderite addition in sodium aluminate solution (Na_2O_k: 230 g/L; α_k: 3.0) at 260 °C

4.5.3 Morphologies of residues from pyrite with goethite and hematite addition

The morphologies of the residues after pyrite digestion with the addition of goethite are shown in Figs. 11(a–d). Numerous fine, spiculated goethite particles were attached to the surface of the pyrite particles, as shown in Fig. 11(a). Similarly, erosive holes with a diameter less than 5 μm were observed on the surface of pyrites at 30 min, resulting from electrochemical corrosion. However, the number of holes was fewer than that observed with siderite addition, as shown in Fig. 10. The addition of goethite also promoted the formation of hematite and magnetite. After 60 min, goethite was no longer observed, whereas octahedral magnetite was clearly present (Area 1). This finding suggests that multiple mechanisms occur after adding goethite into the solution, including the transformation of pyrite into magnetite, goethite into magnetite, and goethite into hematite.

Similarly, after the addition of hematite (Figs. 11(e−h)), rich erosive holes with a diameter of less than 3 μm were also clearly observed on the surface of pyrite (Fig. 9) at 30 min compared to pits after adding goethite in Fig. 11(f), possibly through readily reacting between pyrite and hematite from electrochemical corrosion. From Fig. 11(g), large hematite and magnetite particles were formed. Octahedral magnetite coexisted with a small amount of hematite after 60 min, as observed in Fig. 11(h) (Area 2). These results suggest that $HFeO_2^-$, predominantly formed by reactions with hematite, facilitates the formation of magnetite (Reaction (13) in Table 1).

Therefore, Fe(III) in goethite and hematite, as well as Fe(II) from siderite oxidized to Fe(III), accelerating the pyrite reaction in the sodium aluminate solution through self-oxidation between Fe(III) and S_2^{2-} in FeS_2, leading to rapid magnetite formation. Electrochemical corrosion generates porous pyrite enriched with erosive holes, further accelerating the pyrite reaction. Furthermore, the number of erosive holes in pyrite follows the order of siderite > hematite > goethite, consistent with the reaction efficiencies shown in Fig. 4.

4.6 Effect of iron-bearing minerals on reaction kinetics of pyrite

To further investigate the effect of iron-bearing minerals on the pyrite reaction in the sodium aluminate solution, kinetic models were developed based on nearly constant particle size before and after the reaction (Figs. 2, 9−11), and the concentrated nature of the sodium aluminate solution. Kinetic models were explored from data in Fig. 4 using the surface chemical reaction model (Eq. (3)) and the Kröger and Ziegler model (Eq. (4)) [32], and the results are shown in Fig. 12. Tables S2

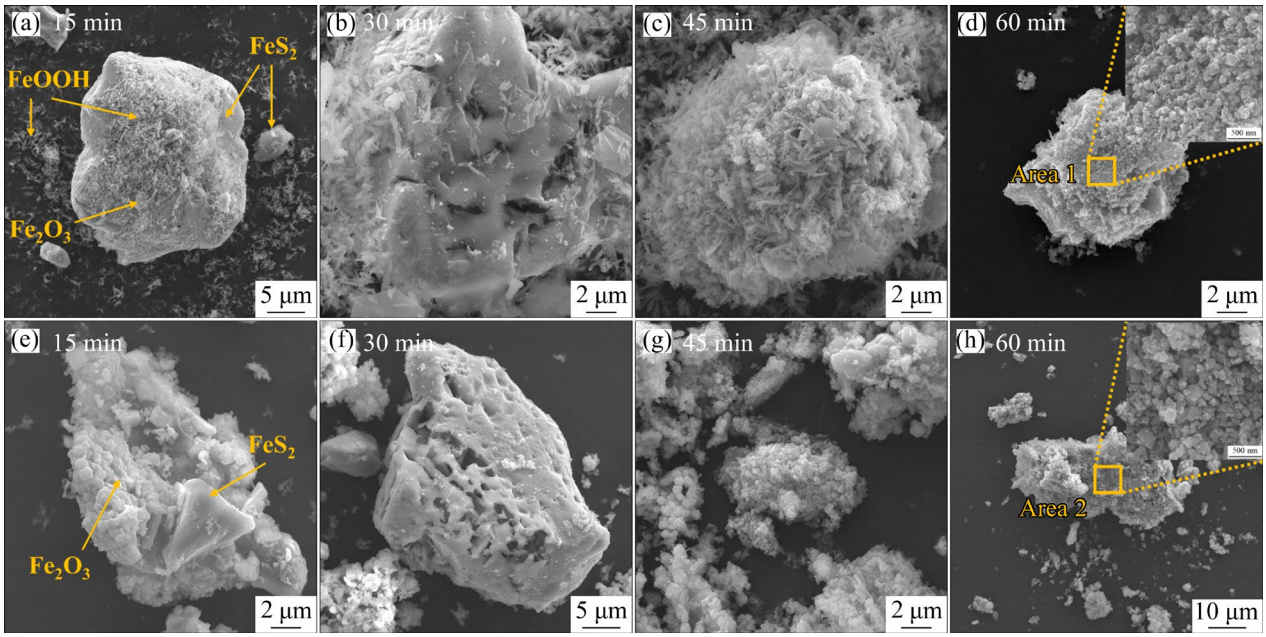

Fig. 11 SEM images of pyrite residues after addition of goethite (a−d) and hematite (e−h) in sodium aluminate solution (Na_2O_k: 230 g/L; α_k: 3.0) at 260 °C

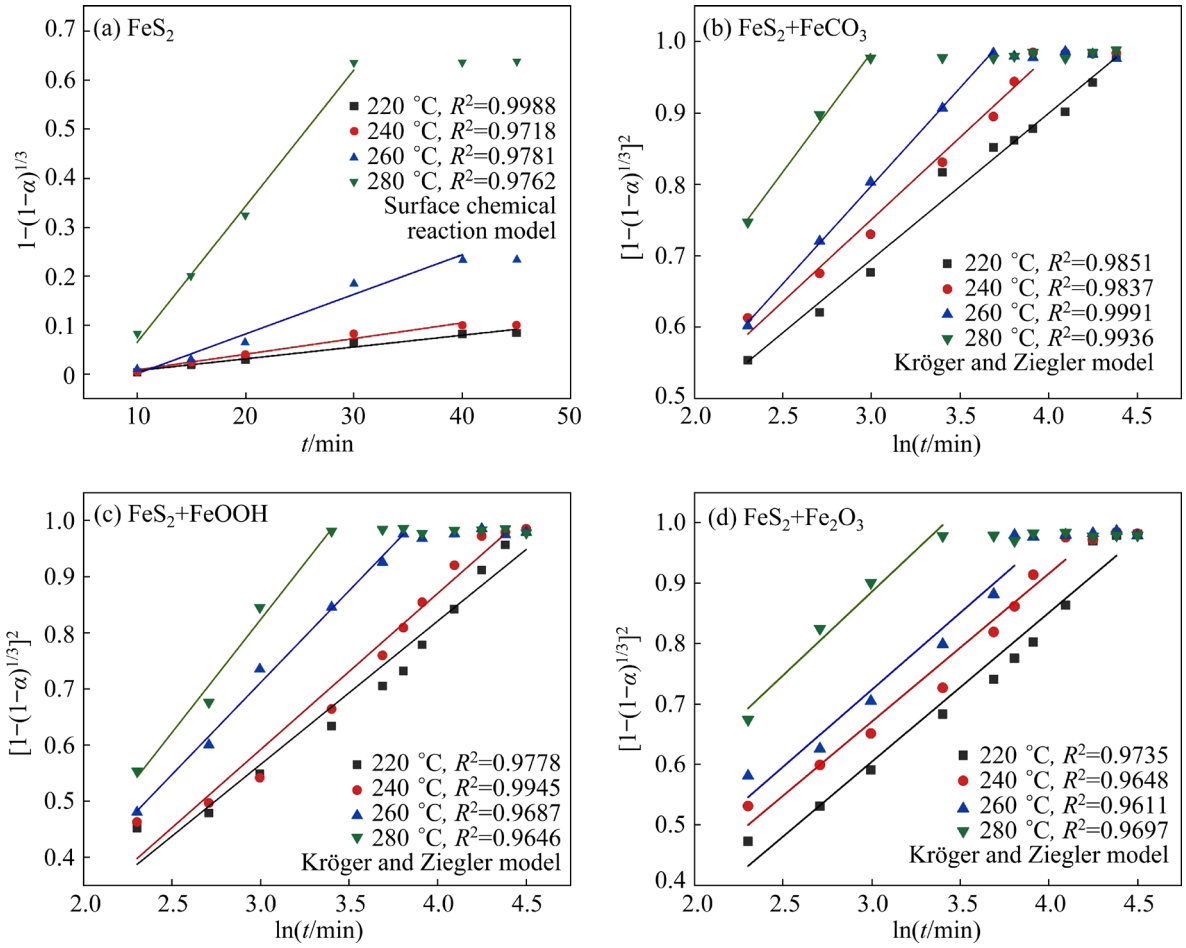

Fig. 12 Effect of iron-bearing minerals on kinetic models of pyrite in sodium aluminate solution (Na_2O_k: 230 g/L, α_k: 3.0)

and S3 in SM present the apparent rate constant k, and correlation coefficient R^2.

The kinetic equations can be rewritten as Eqs. (3) and (4):

$$kt=1-(1-\alpha)^{1/3} \quad (3)$$

$$k\ln t=[1-(1-\alpha)^{1/3}]^2 \quad (4)$$

where t is the reaction time, and α is the reaction extent of pyrite.

As shown in Fig. 12(a) and Tables S2 and S3 in SM, the reaction kinetics of pyrite in the sodium aluminate solution were consistent with the surface chemical reaction model. This suggests that the reaction of pyrite in the sodium aluminate solution is predominantly controlled by chemical reaction [33] within the temperature range of 220−280 °C. Therefore, the reaction of pyrite is mainly temperature-dependent, as shown by the reaction efficiency in Fig. 4.

In contrast, when siderite, goethite, and hematite were added, the reaction kinetics followed the Kröger and Ziegler model (Figs. 12(b−d)), demonstrating that the reactions of pyrite in the sodium aluminate solution are controlled by both interfacial diffusion and chemical reactions. This change is attributed to the occurrence of electrochemical corrosion and the enlarged specific surface area resulting from the formation of erosive holes.

To elucidate the effect of iron-bearing minerals on the reaction mechanism of pyrite, the relationship between $\ln k$ and $1/T$ is plotted in Fig. 13 using the Arrhenius equation (Eq. (5)).

$$k=A\exp[E_a/(RT)] \quad (5)$$

where A is a constant, T is the temperature, and E_a is the apparent activation energy.

Without the addition of iron-bearing minerals, the apparent activation energy of the pyrite reaction

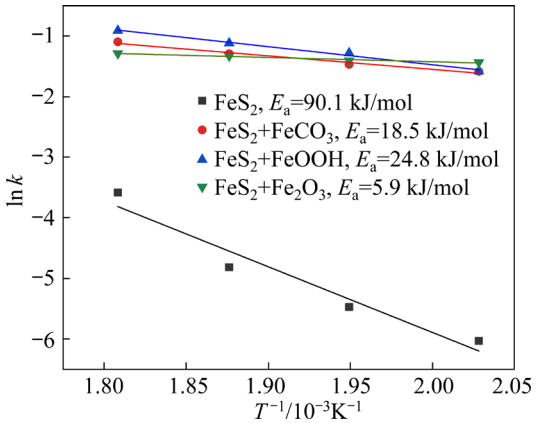

Fig. 13 Relationship between $\ln k$ and $1/T$ based on Arrhenius equation

was 90.1 kJ/mol, consistent with the results from Fig. 12 controlled by the surface chemical reaction. However, after adding siderite, goethite, and hematite, the reaction apparent activation energies decreased significantly to 18.5, 24.8 and 5.9 kJ/mol, respectively. This significant reduction in the apparent activation energies proves that the addition of iron-bearing minerals promotes the pyrite reaction, which aligns well with the results in Figs. 4 and 5 as well as the morphological changes shown in Figs. 10 and 11. The reduction is primarily attributed to electrochemical corrosion and the enlarged specific surface area resulting from erosive holes, which facilitate the diffusion of $HFeO_2^-$ and other ions.

4.7 Self-oxidation mechanism between pyrite and iron-bearing minerals in bauxite

Because pyrite and iron-bearing minerals generally coexist in bauxite, self-oxidation occurs during digestion by the Bayer process, facilitating the removal of sulfur from the solution and iron recovery from the red mud. The reaction mechanism between pyrite and iron-bearing minerals during Bayer digestion is shown in Fig. 14.

Pyrite reacts with sodium aluminate solution to generate S^{2-} and other sulfur anions, along with Fe(II). Only a small amount of Fe(II) was transformed into Fe(III), leading to limited electrochemical reactions, and minimal erosive hole formation. When goethite and hematite are added, Fe(III) from the iron-bearing minerals reacts with S_2^{2-} in pyrite through electrochemical corrosion and oxidation, generating a porous surface enriched with erosive holes and improving the concentrations of $S_2O_3^{2-}$, SO_3^{2-} and SO_4^{2-} with increased R_S. Meanwhile, Fe(II) from siderite rapidly converts to Fe(III), releasing H_2 in the sodium aluminate solution at high temperatures. This results in electrochemical corrosion on the surface of pyrite, generating rich erosive holes. The altered reaction route and improved ion diffusion both accelerate the reaction of pyrite with a low apparent activation energy and promote magnetite formation. Additionally, $HFeO_2^-$ and $Fe(CO_3)_2^{2-}$ both contribute to the high reaction efficiency. The formation of $S_2O_3^{2-}$, SO_3^{2-} and SO_4^{2-}, along with magnetite, supports sulfur removal through desilication and iron recovery from the red mud. However, the role of electrochemical corrosion in forming erosive holes warrants further investigation.

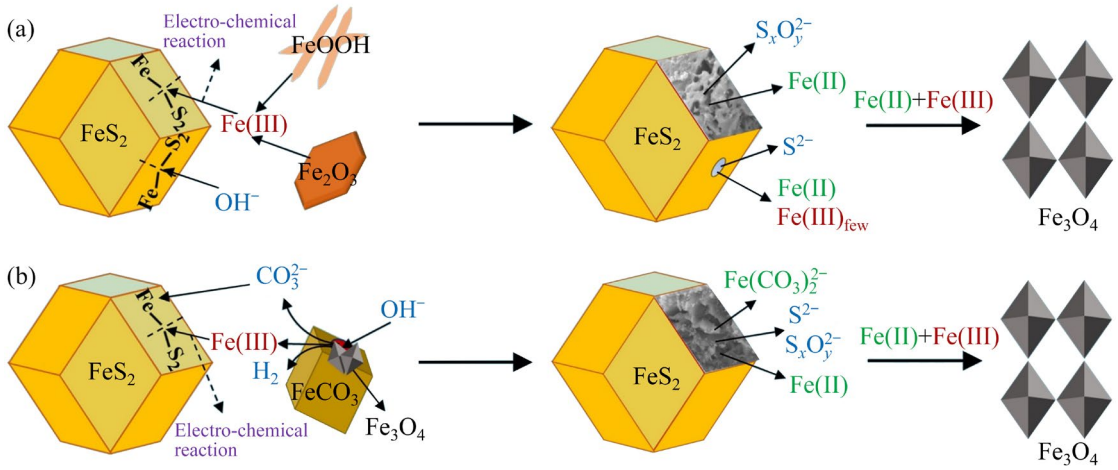

Fig. 14 Schematic of self-oxidation reaction between pyrite and iron-bearing minerals

5 Conclusions

(1) Both Fe(II) and S^{2-} were the predominant species occurred in the sodium aluminate solution following pyrite digestion at high temperatures. The addition of siderite, goethite, and hematite raised the concentration of S^{2-}, S_T, Fe(II) and Fe_T in solution, as well as the increased concentration of $S_2O_3^{2-}$, SO_3^{2-} and SO_4^{2-}.

(2) Siderite, goethite and hematite significantly enhanced the pyrite reaction efficiency in the sodium aluminate solution. Meanwhile, siderite and hematite generated nearly 100% magnetite with more than 72% iron from pyrite at 260 °C for 60 min. Furthermore, these iron-bearing minerals promoted the formation of erosive holes on the pyrite surface through electrochemical corrosion.

(3) The pyrite reaction in the sodium aluminate solution followed the surface chemical reaction model. However, the porous pyrite surface, resulting from electrochemical corrosion, caused the reaction to follow the Kröger and Ziegler model, where interfacial diffusion and chemical reactions governed the process after adding siderite, goethite, and hematite.

CRediT authorship contribution statement

Zhao-hua ZENG: Investigation, Data curation; Writing – Original draft, Writing – Review & editing; **Gui-hua LIU:** Investigation, Conceptualization, Writing – Review & editing, Funding acquisition, Project administration; **Tian-gui QI:** Validation, Funding acquisition; **Lei-ting SHEN:** Supervision, Funding acquisition, Project administration; **Qiu-sheng ZHOU:** Supervision, Validation; **Zhi-hong PENG:** Supervision, Writing – Review & editing; **Yi-lin WANG:** Resources, Supervision; **Xiao-bin LI:** Supervision, Validation.

Declaration of competing interest

The authors declare that they have no known competing financial interests or personal relationships that could have appeared to influence the work reported in this paper.

Acknowledgments

The authors gratefully appreciate the financial support of the National Key R&D Program of China (No. 2022YFC2904404).

Supporting Materials

Supporting Materials in this paper can be found at: https://tnmsc.csu.edu.cn/download/20-p4266-2024-0603-Supporting_Materials.pdf.

References

[1] PHUONG T N T, TSUJI S, JEON S, PARK I, TABELIN C B, ITO M, HIROYOSHI N. Redox potential-dependent chalcopyrite leaching in acidic ferric chloride solutions: Leaching experiments [J]. Hydrometallurgy, 2020, 194: 105299.

[2] AKCIL A, KOLDAS S. Acid mine drainage (AMD): Causes, treatment and case studies [J]. Journal of Cleaner Production, 2006, 14(12/13): 1139−1145.

[3] XU Yong-liang, LIU Yang, BU Yun-chuan, CHEN Meng-lei, WANG Lan-yun. Review on the ionic liquids affecting the desulfurization of coal by chemical agents [J]. Journal of Cleaner Production, 2021, 284: 124788.

[4] PAN Xiao-lin, WU Hong-fei, LV Zhong-yang, YU Hai-yan, TU Gan-feng. Recovery of valuable metals from red mud: A comprehensive review [J]. Science of the Total Environment, 2023, 904: 166686.

[5] CHENG G, LI Y L, ZHANG M N. Research progress on desulfurization technology of high-sulfur bauxite [J]. Transactions of Nonferrous Metals Society of China, 2022, 32(10): 3374−3387.

[6] LIU Zhan-wei, LI Dun-yong, MA Wen-hui, YAN Heng-wei, XIE Ke-qiang, ZHENG Li-cong, LI Peng-fei. Sulfur removal by adding aluminum in the Bayer process of high-sulfur bauxite [J]. Minerals Engineering, 2018, 119: 76−81.

[7] LIU Zhan-wei, MA Wen-hui, YAN Heng-wei, XIE Ke-qiang, LI Dun-yong, ZHENG Li-cong, LI Peng-fei. Removal of sulfur by adding zinc during the digestion process of high-sulfur bauxite [J]. Scientific Reports, 2017, 7(1): 17181.

[8] LI Xiao-bin, NIU Fei, TAN Jie, LIU Gui-hua, QI Tian-gui, PENG Zhi-hong, ZHOU Qiu-sheng. Removal of S^{2-} ion from sodium aluminate solutions with sodium ferrite[J]. Transactions of Nonferrous Metals Society of China, 2016, 26(5): 1419−1424.

[9] HE Run-de. Sulphur removal with barium hydroxide from industrial sodium aluminate solution [J]. Nonferrous Metals, 1996(4): 64−67. (in Chinese)

[10] CHUANG K C, CHEN M C, GREER R T, MARKUSZEWSKI R, SUN Y, WHEELOCK T D. Pyrite desulfurization by wet oxidation in alkaline solutions [J]. Chemical Engineering Communications, Taylor & Francis, 1980, 7(1/2/3): 79−94.

[11] LIU Shu-xin, LIU Zhan-wei, YAN Heng-wei, LI Meng-nan, XIA Cheng-cheng. Desulfurization by adding sodium nitrate in the production of alumina from high-sulfur bauxite [J]. JOM, 2023, 75(5): 1649−1659.

[12] LI Xiao-bin, XI Ya-wei, WANG Yi-lin, QI Tian-gui, LIU Gui-hua, ZHOU Qiu-sheng, PENG Zhi-hong. Formation and transformation mechanism of sulfur-containing desiliconization products under simulated Bayer digestion conditions [J]. The Chinese Journal of Nonferrous Metals, 2020, 30(8): 1906−1914. (in Chinese)

[13] SINGER P C, STUMM W. Acidic mine drainage: The rate-determining step [J]. Science, 1970, 167(3921): 1121−1123.

[14] TABELIN C B, CORPUZ R D, IGARASHI T, VILLACORTE-TABELIN M, ALORRO R D, YOO K, RAVAL S, ITO M, HIROYOSHI N. Acid mine drainage formation and arsenic mobility under strongly acidic conditions: Importance of soluble phases, iron

oxyhydroxides/oxides and nature of oxidation layer on pyrite [J]. Journal of Hazardous Materials, 2020, 399: 122844.
[15] SONG Chao, PENG Zhi-hong, WEI Xin-xin, QI Tian-gui. The reaction behavior of pyrite in the process of Bayer digestion [J]. Nonferrous Metals Science and Engineering, 2011, 2(5): 1−5. (in Chinese)
[16] LIU Gui-hua, GAO Jun-li, LI Xiao-bin, XU Shuang. Study on variation rule of iron in the aluminate solution after digestion process at high temperature by Bayer process [J]. Mining and Metallurgical Engineering, 2007, (5): 38−40. (in Chinese)
[17] WANG Sai-kui, WANG Yi-lin, LI Mu-zhou, QI Tian-gui, LIU Gui-hua, ZHOU Qiu-sheng, PENG Zhi-hong, LI Xiao-bin. Characteristics of product layer and effects of sulfur-bearing ions on pyrite leaching in sodium aluminate solutions [J]. Minerals Engineering, 2023, 202: 108295.
[18] LI Xiao-bin, LIU Nan, QI Tian-gui, WANG Yi-lin, ZHOU Qiu-sheng, PENG Zhi-hong, LIU Gui-hua. Conversion of ferric oxide to magnetite by hydrothermal reduction in Bayer digestion process [J]. Transactions of Nonferrous Metals Society of China, 2015, 25(10): 3467−3474.
[19] SONG Shu-qing, LIU Gui-hua, WANG Xiao-yang, QI Tian-gui, SHEN Lei-ting, PENG Zhi-hong. Rule and mechanism of goethite changing into hematite in sodium aluminate solution with a low concentration of iron [J]. The Chinese Journal of Nonferrous Metals, 2023, 33(6): 1935−1946. (in Chinese)
[20] CIMINELLI V S T, OSSEO-ASARE K. Kinetics of pyrite oxidation in sodium carbonate solutions [J]. Metallurgical and Materials Transactions B, 1995, 26(2): 209−218.
[21] LI Xiao-bin, NIU Fei, LIU Gui-hua, QI Tian-gui, ZHOU Qiu-sheng, PENG Zhi-hong. Effects of iron-containing phases on transformation of sulfur-bearing ions in sodium aluminate solution [J]. Transactions of Nonferrous Metals Society of China, 2017, 27(4): 908−916.
[22] AL-JAROUDI S S, UL-HAMID A, MOHAMMED A I, SANER S. Use of X-ray powder diffraction for quantitative analysis of carbonate rock reservoir samples [J]. Powder Technology, 2007, 175(3): 115−121.
[23] LI Xiao-bin, LI Chong-yang, ZHOU Qiu-sheng, QI Tian-gui, LIU Gui-hua, PENG Zhi-hong. Interaction of sodium sulfide with silica-containing minerals in sodium aluminate solution [J]. International Journal of Mineral Processing, 2015, 137: 9−14.
[24] WANG Sai-kui, WANG Yi-lin, QI Tian-gui, LIU Gui-hua, ZHOU Qiu-sheng, PENG Zhi-hong, NIU Fei, LI Xiao-bin. Effect of redox agents on the reaction behavior of pyrite in sodium aluminate solution at elevated temperatures [J]. Minerals Engineering, 2023, 191: 107974.
[25] KOLTHOFF I M, SANDELL E B. Textbook of quantitative inorganic analysis [M]. New York: Macmillan, 1952.
[26] JAMES G S. Lange's handbook of chemistry [M]. New York: McGraw-Hill Education, 2017.
[27] LIU Zhan-wei, LI Wang-xing, MA Wen-hui, YIN Zhong-lin, WU Guo-bao. Conversion of sulfur by wet oxidation in the Bayer process [J]. Metallurgical and Materials Transactions B, 2015, 46(4): 1702−1708.
[28] NIU Fei, LI Xiao-bin, ZHOU Qiu-sheng, QI Tian-gui, LIU Gui-hua, PENG Zhi-hong. Variation of mass concentration of iron in sulfur sodium aluminate solution [J]. Journal of Central South University (Science and Technology), 2015, 46(12): 4398−4403. (in Chinese)
[29] ZHOU Xue-jiao, TAN Fei, CHEN Yong-li, YIN Jian-guo, XIA Wen-tang, HUANG Qing-yun, GAO Xu-dong. Thermodynamic analysis of Na−S−Fe−H_2O system for Bayer process [J]. Transactions of Nonferrous Metals Society of China, 2022, 32(6): 2046−2060.
[30] CALDEIRA C L, CIMINELLI V S T, OSSEO-ASARE K. The role of carbonate ions in pyrite oxidation in aqueous systems [J]. Geochimica et Cosmochimica Acta, 2010, 74(6): 1777−1789.
[31] BIERNAT R J, ROBINS R G. High-temperature potential/pH diagrams for the iron−water and iron−water−sulphur systems [J]. Electrochimica Acta, 1972, 17(7): 1261−1283.
[32] DICKINSON C F, HEAL G R. Solid−liquid diffusion controlled rate equations [J]. Thermochimica Acta, 1999, 340/341: 89−103.
[33] BURKIN A R, EDWARDS A M. The formation of insoluble iron oxide coatings during the alkali pressure leaching of pyrite [C]//Proceedings of 6th International Congress of Mineral Processing. Cannes, France: BRGM, 1963, 26: 159−167.

含铁矿物之间的自氧化促进黄铁矿在拜耳液中生成磁铁矿

曾昭华，刘桂华，齐天贵，申雷霆，周秋生，彭志宏，王一霖，李小斌

中南大学 冶金与环境学院，长沙 410083

摘　要：基于铝土矿中黄铁矿与含铁矿物共存的特点，研究了菱铁矿、赤铁矿和针铁矿在高温铝酸钠溶液中对黄铁矿反应的影响。菱铁矿、针铁矿和赤铁矿的加入提高了 $S_2O_3^{2-}$、SO_3^{2-}和 SO_4^{2-}的浓度，这有利于脱硅过程中硫的脱除。菱铁矿和赤铁矿与黄铁矿生成了近 100%的磁铁矿，而针铁矿则通过多相转化过程与黄铁矿生成赤铁矿和磁铁矿，从而显著提高了渣中铁的含量和赤泥中铁的回收率。菱铁矿、针铁矿和赤铁矿在电化学腐蚀作用下以侵蚀孔的形式使得黄铁矿形成多孔表面，从而提高了黄铁矿的反应效率。此外，在菱铁矿、赤铁矿和磁铁矿存在的条件下，电化学腐蚀导致黄铁矿的反应遵循 Kröger 和 Ziegler 模型，受界面扩散和化学反应双重控制。

关键词：黄铁矿；自氧化；含铁矿物；磁铁矿；铝酸钠溶液

(Edited by Xiang-qun LI)